Multiple Scattering Model for Beam Synthesis With Reconfigurable Intelligent Surfaces

Tommi E. Rimpiläinen and Riku Jäntti, *Senior Member, IEEE*

***Abstract*— This article presents a method of synthetic beamforming for reconfigurable intelligent surfaces (RIS). The method uses a T-matrix-based multiple scattering model to compute the scattering from the RIS. We assume that the elements of the RIS are infinite circular cylinders. This allows us to make the model 2-D. Furthermore, we assume that the RIS elements satisfy the impedance boundary condition (IBC), the complex parameter of which adjusts the phase shift of the scattered field. We synthesize the beam both analytically and numerically. Both approaches rely on an approximation that assumes RIS elements that are small compared to the wavelength. We demonstrate the efficacy of the beam synthesis by applying it in a test case that features a linear array of RIS elements.**

***Index Terms*— Beam steering, boundary conditions, reconfigurable intelligent surfaces (RIS), surface impedance.**

I. Introduction

MODERN telecommunication technologies use advanced physical layer components that allow the services to adapt to changing situations in real-time. If several transceivers are available in the environment, the service can adapt to changes by adjusting the emitted signals of the transceivers. However, if suitable components are used, the service can fine-tune itself according to the demands of the situation, even without an extensive set of transceivers, by adjusting the propagation environment instead of the emitted signal [1], [2]. The important distinction is that the propagation environment can be adjusted by using passive elements that are relatively inexpensive and therefore scalable. A component that holds particular promise in passively adjusting the propagation environment is the *reconfigurable intelligent surface* (RIS). A surface is a versatile tool that can be deployed in several ways—even embedded inside a wallpaper.

Although RIS has been studied extensively in the literature [3], [4], [5], [6], [7], [8], [9], [10], [11], [12], the existing literature tends to focus on the far region of the RIS. It is also possible to model the RIS with scattering parameter network analysis—treating the wireless channel as a linear multiport network [13]. This approach avoids an explicit discussion of the physical propagation mechanism of electromagnetic fields. Although relatively little has been written about modeling the electromagnetic fields of the RIS in the near region [14], [15], [16], the near region is essential for many prospective applications of the RIS. This is the case, for example, when an RIS covers a significant portion of a wall inside a room in which measurements are conducted. Therefore, this article uses a propagation model that is valid in both the near region of the reflecting surface and in the far region. Moreover, the model is not only valid in the near region of the surface, but also in the near regions of the individual RIS elements. It is necessary to know the near-region electromagnetic response precisely when we aim to accurately model the interactions between the RIS elements.

This article considers a particular use case of RIS. The goal is to use the surface as a reflector element in a reflector antenna, where the receiver element is too small to achieve a high directivity by itself but is able to focus its beam sharply with the aid of the reflecting surface (Fig. 5). We refer to this kind of reflector antenna as an *RIS augmented receiver*. An important distinction to an ordinary reflector antenna is that the beam of the augmented receiver can easily be steered in real time without physically rotating the antenna. In this respect, the augmented receiver more resembles an antenna array than an ordinary reflector antenna.

To study the properties of the RIS-augmented receiver, we use an idealized 2-D electromagnetic propagation model. In the model, the scattering elements of the RIS are taken to be infinitely long circular cylinders, the axes of which are all oriented in the same direction. To make these cylinders serve as the elements of an RIS, we design the cylinders in a way that allows them to scatter a signal-carrying electric field with a given amount of delay. The delayed scattering is modeled with an electromagnetic boundary condition that implements a customized phase shift. For this purpose, the *impedance boundary condition* (IBC) proves suitable (Section III-A).

Because the RIS elements are assumed circular, the impinging electromagnetic field scatters in all directions from each element. Therefore, part of the scattered field of a given element impinges another element in the array. As the mechanism repeats, the initial scattered field is further scattered several times in a process of *multiple scattering* [17]. When we design the RIS-augmented receiver, it is important to account for the multiple scattering processes because the field that the receiver element of the augmented receiver registers is a combination of the directly impinging plane wave and the field that the RIS elements passively produce by multiple scattering.

Manuscript received 2 December 2022; revised 15 February 2023; accepted 14 March 2023. Date of publication 3 April 2023; date of current version 2 June 2023. This work was supported by the Academy of Finland through Backscatter enabled sustainable monitoring Infrastructure for assisted living (BESIMAL) Project under Grant 334197. *(Corresponding author: Tommi E. Rimpiläinen.)*

The authors are with the Department of Information and Communications Engineering, School of Electrical Engineering, Aalto University, 00076 Aalto, Finland (e-mail: tommi.e.rimpilainen@aalto.fi; riku.jantti@aalto.fi).

Color versions of one or more figures in this article are available at https://doi.org/10.1109/TAP.2023.3262638.

Digital Object Identifier 10.1109/TAP.2023.3262638

Typical implementations of an RIS can adjust the phase shifts of the RIS elements only in discrete steps, rather than continuously [8]. This design limitation is relevant when the RIS-augmented receiver is used for beamforming. Because of the design limitation, the orientations of the mainlobes that the augmented beamformer can implement are generally all different from the desired orientation, so the beam cannot be steered in the correct direction. However, we can synthesize a beam in any direction using the discrete set of beams that the augmented receiver gives. A novel method of *beam synthesis* is introduced in Section IV-B.

In sum, the contributions of the present article are the following.

1) An RIS is implemented with IBC cylinders (Section III-A).
2) An RIS is modeled with the theory of electromagnetic multiple scattering (Section III-B).
3) With an RIS based on IBC cylinders, beam synthesis is demonstrated (Sections IV and V).
4) The full-wave electromagnetic field theory is applicable both in the near region of the RIS and in the far region, which allows us to study the near-region electromagnetic response of the RIS in a situation where the primary field source is distant (Section IV).

These contributions are novel, so far as the authors are aware.

II. Matrix Conventions

We follow some well-established conventions of matrix notation throughout the article for clarity of representation. We use capital letters of the bold typeface, like $\mathbf{T}$ or $\mathbf{Q}$, to denote matrices. We use lower case letters of the bold typeface, like $\mathbf{a}$ or $\mathbf{v}_\mathbf{k}$, to denote column vectors. We use the vector transpose $\boldsymbol{\kappa}^T$ or the Hermitian transpose $\mathbf{w}^H = (\mathbf{w}^T)^*$ when we refer to row vectors. We denote a column vector of unit elements by $\mathbb{1}$. A matrix with elements a_{ij} is denoted $[a_{ij}]$. Likewise, a matrix with column vectors $\mathbf{a}_n$ is denoted $[\mathbf{a}_n]$. A diagonal matrix with diagonal entries from a vector $\mathbf{a}$ is denoted by $\mathrm{diag}(\mathbf{a})$.

A given vector norm $\|\cdot\|$ induces a matrix norm by the following equation:

$$\|\mathbf{A}\| = \sup_{\mathbf{x}\neq 0} \frac{\|\mathbf{A}\mathbf{x}\|}{\|\mathbf{x}\|}.$$

We leave unspecified the variety of the vector norm, so that the norm can be, for example, the taxicab norm or the Euclidean norm. The condition number of an invertible matrix is

$$\mathrm{cond}(\mathbf{A}) = \|\mathbf{A}\|\|\mathbf{A}^{-1}\|$$

and this is submultiplicative

$$\mathrm{cond}(\mathbf{AB}) \leq \mathrm{cond}(\mathbf{A})\,\mathrm{cond}(\mathbf{B}). \tag{1}$$

The Kronecker delta function is

$$\delta_{ij} = \begin{cases} 1, & \text{if } i = j \\ 0, & \text{otherwise} \end{cases} \tag{2}$$

and the identity matrix is $\mathbf{I} = [\delta_{ij}]$.

III. Propagation Model

A. Delayed Scattering

An individual scattering element is assumed to be an infinite circular cylinder of radius R, oriented along the z-axis of the Cartesian coordinate system. We consider the case where the impinging field is a time-harmonic *transverse magnetic* field of an angular frequency ω, that is, of the form $\mathbf{E}_z^i(\mathbf{r},\mathbf{t}) = \mathbf{u}_z E_z^i(\mathbf{r}) e^{-i\omega t}$. The circular shape of the scatterer makes it convenient to represent the impinging field E_z^i and the scattered field E_z^s in the polar coordinate system $\mathbf{r} = (r\cos\varphi, r\sin\varphi, z)$ centered on the cylinder. The right-handed basis $(\mathbf{u}_r, \mathbf{u}_\varphi, \mathbf{u}_z)$ of the coordinate system at a given point $\mathcal{P}$ consists of unit vectors along the coordinate lines of r, φ, and z, respectively, through $\mathcal{P}$ (Fig. 1). The rectangular components of $\mathbf{E}_z^i$ and $\mathbf{E}_z^s$ satisfy the scalar Helmholtz equation

$$\nabla^2\psi + k^2\psi = 0 \tag{3}$$

where the wavenumber k depends on the material where the cylinder is embedded. We assume that the material is linear, homogeneous, and isotropic, so that k is a scalar of a constant value. Then, by linearity, the total field $E_z = E_z^i + E_z^s$ satisfies (3) whenever E_z^i and E_z^s do. In the polar coordinate system, the solutions of (3) feature the Bessel function $J_n(kr)$ and the Hankel function $H_n(kr)$ of the first kind. In particular, the waveforms

$$\psi_n(\mathbf{r}) = H_n(kr)e^{in\varphi}, \quad \hat{\psi}_n(\mathbf{r}) = J_n(kr)e^{in\varphi} \tag{4}$$

are known to satisfy the scalar Helmholtz equation [18, Sec. 6.6].

An important qualitative distinction between $J_n(kr)$ and $H_n(kr)$ is that $J_n(kr)$ remains regular near the axis $r = 0$ of the cylindrical coordinates, while $H_n(kr)$ becomes singular at the axis but remains regular at great distances. The physical significance of this distinction is that, in (4), the waveforms $\psi_n(\mathbf{r})$ reduce asymptotically to outward traveling plane waves and therefore conveniently represent the outbound fields, whereas the waveforms $\hat{\psi}_n(\mathbf{r})$ represent the impinging fields. At a given distance r from the center of the cylinder, the impinging field is a function of the cyclic coordinate φ and can therefore be expanded as a Fourier series

$$E_z^i(r,\varphi) = \sum_{n=-\infty}^{\infty} a_n J_n(kr)e^{in\varphi} = \sum_{n=-\infty}^{\infty} a_n \hat{\psi}_n(\mathbf{r}). \tag{5}$$

Similarly, the expansion

$$E_z^s(r,\varphi) = \sum_{n=-\infty}^{\infty} b_n H_n(kr)e^{in\varphi} = \sum_{n=-\infty}^{\infty} b_n \psi_n(\mathbf{r}) \tag{6}$$

is valid for the outbound field.

Because we want to model phase-shifted scattering, we need to consider a cylinder with a boundary condition that can be suitably customized to effect the required shift. We, therefore, consider a cylindrical surface on which the IBC applies. The isotropic IBC [19, Ch. 3] is

$$\mathbf{E}_t = Z(\mathbf{n}\times\mathbf{H}_t) \tag{7}$$

where $\mathbf{E}_t$ and $\mathbf{H}_t$ are the components of the electric and the magnetic field that are tangential to the boundary surface,

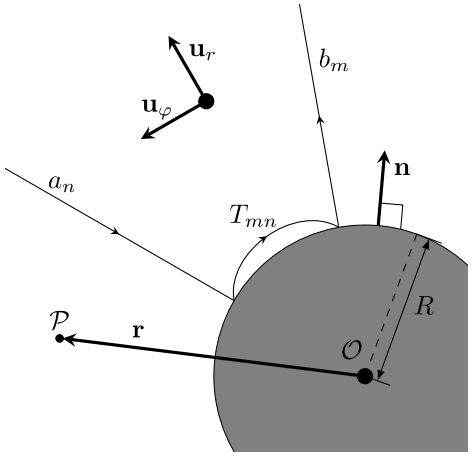

Fig. 1. Scattering from a circular IBC cylinder. The coefficients b_m of the outbound waveforms are a weighed sum $\sum T_{mn}a_n$ of the coefficients of the impinging waveforms, by linearity. However, it follows from the symmetry of the geometry that $T_{mn} = 0$ when $m \neq n$. Delay can be introduced into the scattered field by adjusting the complex phase of the remaining coefficients T_{mm}. We can adjust the complex phase of T_{mm} by changing the IBC parameter ξ in (10). When the inclusion is small, only T_{00} is important. The vector $\mathbf{u}_z = \mathbf{u}_r \times \mathbf{u}_\varphi$ is oriented at right angles to the plane of the drawing.

respectively, Z is a given parameter—referred to as the *boundary impedance*—and $\mathbf{n}$ is the unit normal vector of the surface (Fig. 1). For the particular orientation of the impinging and outbound fields, we have

$$\mathbf{H}_t = H_\varphi \mathbf{u}_\varphi = -\frac{1}{i\omega\mu}\frac{\partial E_z}{\partial r}\mathbf{u}_\varphi \tag{8}$$

where μ is the permeability of the medium. The IBC (7) can, therefore, be expressed in terms of the electric field and its radial derivative, so that

$$E_z + \xi\frac{\partial E_z}{\partial r} = 0, \qquad \text{where } \xi \triangleq \frac{Z}{i\omega\mu}. \tag{9}$$

When we impose this condition at the cylinder boundary $r = R$, we find from (5) and (6) and from $E_z = E_z^i + E_z^s$ that the coefficients a_n and b_n are related by the following equation:

$$b_n = -\frac{J_n(kR) + \xi\frac{\partial}{\partial r}J_n(kR)}{H_n(kR) + \xi\frac{\partial}{\partial r}H_n(kR)}a_n = T_{nn}a_n \tag{10}$$

where we define T_{nn} as the factor that relates the amplitude of a given component of the impinging field to the corresponding component of the scattered field. From (10), we see that the factors T_{nn} only depend on the boundary condition and the geometry of the scatterer and not on the impinging field. If we combine the coefficients into column vectors of infinite length, so that

$$\begin{aligned}\mathbf{a} &= [a_n]\\ \mathbf{b} &= [b_n]\end{aligned} \tag{11}$$

we see that the coefficients b_n of the outbound field are given for all impinging fields by the following equation:

$$\mathbf{b} = \mathbf{T}\mathbf{a} \tag{12}$$

where $\mathbf{T}$ is an infinite diagonal matrix with the elements T_{nn} at its diagonal. Matrix $\mathbf{T}$ is referred to as the T-matrix of the scatterer. In computation, $\mathbf{T}$ is truncated to a suitable size.

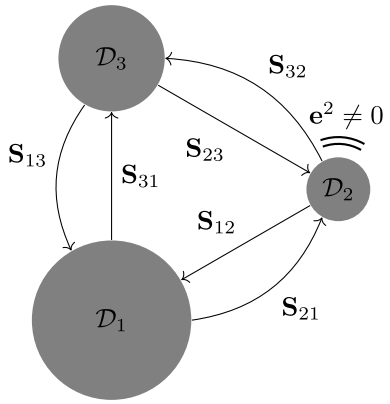

Fig. 2. Multiple scattering between IBC cylinders. The radii R_j and the parameters ξ_j of the boundary condition can vary between the objects. Also, some of the objects can be active, with positive emission $\mathbf{e}^j$.

The perfectly conducting cylinder—with vanishing E_z at the surface—is given as the special case, $\xi = 0$. It is convenient to compare the phase shift of the more general IBC cylinder to that of the perfectly conducting cylinder. Although the scattered field of an IBC cylinder generally differs from the phase-shifted scattered field of a perfectly conducting cylinder, the two fields nearly coincide when both cylinders are sufficiently small, because at this limit the b_0 coefficient in (10) becomes dominant over the other coefficients b_n. That the coefficient b_0 of the monopole waveform dominates can be seen from the asymptotic behavior of $H_0(kR)$ as $R \to 0$ [20, eq. (10.7.2)] or by observing that a small cylinder is unable to support a long multipole axis [21, eq. (5.131)]. When we truncate the series in (6) to include only the b_0 term, we refer to this as the *small element approximation*. We obtain the value ξ of the IBC parameter that corresponds to a phase shift ϕ when we, in (10), treat b_0 as a function of ξ and require that $b_0(\xi) = e^{i\phi}b_0(0)$. Explicitly, we solve

$$\frac{J_0(kR)}{H_0(kR)}e^{i\phi} = \frac{J_0(kR) + \xi\frac{\partial}{\partial r}J_0(kR)}{H_0(kR) + \xi\frac{\partial}{\partial r}H_0(kR)}. \tag{13}$$

We can then find the remaining values T_{nn} directly from (10).

If the radius of the cylinder is greater than the wavelength, the cylinder can no longer be regarded as sufficiently small to allow an approximation that only involves b_0. In that case, the phase shift depends on the propagation direction of the scattered field. For simplicity, we calculate the boundary parameter ξ assuming that the phase shift is nearly isotropic. Because (5) and (6) provide the precise magnitude and phase of the fields independent of the approximation, the conclusions of the present article do not critically depend on the accuracy of the approximation. The accuracy of the approximation merely determines the precision with which a given phase shift ϕ can be implemented with the boundary parameter ξ. This implementation need not be precise for the present purposes.

B. Multiple Scattering

The RIS elements of the augmented receiver have the primary purpose of scattering the electromagnetic fields that impinge them to the receiver element. However, the RIS

elements also scatter one another. We, therefore, have to account for the resulting multiple scattering processes.

We amend our notation to accommodate several objects $\mathcal{D}_j$ by denoting with $\mathbf{a}^j$ and $\mathbf{b}^j$ the vectors that hold the coefficients of the impinging waveforms $\hat{\psi}_n^j$ and the outbound waveforms ψ_m^j. Because the objects that we consider observe the IBC, it follows that the electric response of the objects is linear, so a T-matrix representation $\mathbf{T}^j\mathbf{a}^j$ gives the coefficients of the scattered field of a given object $\mathcal{D}_j$. The coefficients $\mathbf{b}^j$ of the outbound waveforms are the sum of the coefficients of the scattered field and the coefficients $\mathbf{e}^j$ of the emitted field, so that

$$\mathbf{b}^j = \mathbf{e}^j + \mathbf{T}^j\mathbf{a}^j. \tag{14}$$

When N objects $\mathcal{D}_1, \mathcal{D}_2, \ldots, \mathcal{D}_N$ are present, the multiple T-matrix expressions can be bundled into a single block matrix expression

$$\begin{pmatrix} \mathbf{b}^1 \\ \mathbf{b}^2 \\ \vdots \\ \mathbf{b}^N \end{pmatrix} = \begin{pmatrix} \mathbf{e}^1 \\ \mathbf{e}^2 \\ \vdots \\ \mathbf{e}^N \end{pmatrix} + \begin{pmatrix} \mathbf{T}^1 & & & 0 \\ & \mathbf{T}^2 & & \\ & & \ddots & \\ 0 & & & \mathbf{T}^N \end{pmatrix} \begin{pmatrix} \mathbf{a}^1 \\ \mathbf{a}^2 \\ \vdots \\ \mathbf{a}^N \end{pmatrix}$$

which we will write more briefly as follows:

$$\mathbf{b} = \mathbf{e} + \mathbf{T}\mathbf{a}. \tag{15}$$

We also need to model the physics of wave propagation to arrive at a system of equations from which $\mathbf{a}$ and $\mathbf{b}$ can be determined uniquely (Fig. 2). Assuming that all sources are explicit—that is, there are no sources that are external to all the objects $\mathcal{D}_j$—and that the objects have no self-interactions, the impinging field of a given object is the same as the combined scattered and emitted fields of all the other objects in the environment. Again, linearity implies that the wave propagation from objects $\mathcal{D}_1, \ldots, \mathcal{D}_N$ to object $\mathcal{D}_i$ has the general form

$$\mathbf{a}^i = \sum_{j \neq i} \mathbf{S}^{ij}\mathbf{b}^j \tag{16}$$

which in the block matrix notation is

$$\begin{pmatrix} \mathbf{a}^1 \\ \mathbf{a}^2 \\ \vdots \\ \mathbf{a}^N \end{pmatrix} = \begin{pmatrix} 0 & \mathbf{S}^{12} & \ldots & \mathbf{S}^{1N} \\ \mathbf{S}^{12} & 0 & & \mathbf{S}^{2N} \\ \vdots & & \ddots & \vdots \\ \mathbf{S}^{N1} & \mathbf{S}^{N2} & \ldots & 0 \end{pmatrix} \begin{pmatrix} \mathbf{b}^1 \\ \mathbf{b}^2 \\ \vdots \\ \mathbf{b}^N \end{pmatrix} \tag{17}$$

or in brief

$$\mathbf{a} = \mathbf{S}\mathbf{b} \tag{18}$$

where the elements of the matrix $\mathbf{S}$ only depend on the relative positions of the objects $\mathcal{D}_i$. When we combine (15) and (18), we obtain

$$\begin{aligned} (\mathbf{I} - \mathbf{S}\mathbf{T})\mathbf{a} &= \mathbf{S}\mathbf{e} \\ (\mathbf{I} - \mathbf{T}\mathbf{S})\mathbf{b} &= \mathbf{e} \end{aligned} \tag{19}$$

from which vectors $\mathbf{a}$ and $\mathbf{b}$ can be separately solved with numerical linear algebra.

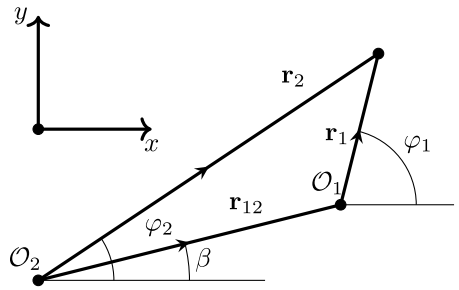

Fig. 3. Addition theorem. An outbound waveform $\psi_n(\mathbf{r}_2)$, which is referred to the origin $\mathcal{O}_2$, can be expressed as a sum of impinging waveforms $\hat{\psi}_n(\mathbf{r}_1)$, which are referred to $\mathcal{O}_1$.

The matrix $\mathbf{S}^{12}$ is obtained by employing a theorem that connects the waveforms that propagate outward from a given point $\mathcal{O}_2$ to the waveforms that propagate inward toward another point $\mathcal{O}_1$. The required theorem is the Graf theorem [17, eq. (2.25)], which states that

$$\psi_n(\mathbf{r}_2) = \sum_{m=-\infty}^{\infty} \psi_{n-m}(\mathbf{r}_{12})\hat{\psi}_m(\mathbf{r}_1) \tag{20}$$

for $r_1 < r_{12}$. Here, $\mathbf{r}_{12}$ is the vector from $\mathcal{O}_2$ to $\mathcal{O}_1$ (Fig. 3). We find the coefficients of $\mathbf{S}^{12}$ when we require that (18) holds for all vectors $\mathbf{b}$. We can then set $\mathbf{b}^j = 0$ for all $j \neq 2$. In this special case, the field that impinges $\mathcal{D}_1$ is precisely the field that is transmitted by $\mathcal{D}_2$, so that in the neighborhood of $\mathcal{D}_1$, we have

$$\begin{aligned} \sum_{l=-\infty}^{\infty} b_l\psi_n(r_2) &= \sum_{m=-\infty}^{\infty} a_m\hat{\psi}_m(r_1) \\ &= \sum_{m=-\infty}^{\infty}\sum_{l=-\infty}^{\infty} S_{ml}^{12}b_l\hat{\psi}_m(r_1). \end{aligned} \tag{21}$$

Because the equation holds for all $\mathbf{b}$, we can set $b_l = \delta_{nl}$, so that all coefficients b_l vanish except for the coefficient $b_n = 1$. We then have

$$\psi_n(\mathbf{r}_2) = \sum_{m=-\infty}^{\infty} S_{mn}^{12}\hat{\psi}_m(\mathbf{r}_1) \tag{22}$$

so that $S_{mn}^{12} = \psi_{n-m}(\mathbf{r}_{12})$, by a comparison with (20), and more generally

$$S_{mn}^{ij} = \psi_{n-m}(\mathbf{r}_{ij}) \tag{23}$$

where $\mathbf{r}_{ij}$ is the vector from $\mathcal{O}_j$ to $\mathcal{O}_i$.

Sources that are located at a significant distance from other objects in the scattering problem may be treated as sources of ideal plane waves. They feature in matrices $\mathbf{T}$ and $\mathbf{S}$ in a specialized way. Because the sources are far apart from the other objects, we assume that their scattering can be neglected in $\mathbf{T}$. Because the exact location of a plane-wave source is not usually known, we take the vector $\mathbf{r}_{12}$ to be a vector that reaches $\mathcal{O}_1$ from some arbitrary location $\mathcal{O}_2$, where the plane wave has a complex value $E_z(\mathbf{r}) = e_e$. If the plane wave propagates in the direction given by the unit vector $\hat{\mathbf{k}}$, its wave vector is $\mathbf{k} = k\hat{\mathbf{k}}$. The same plane wave can be referred to

as the origin $\mathcal{O}_1$ and the origin $\mathcal{O}_2$. This gives two different representations that are connected by the following equation:

$$e_e e^{i\mathbf{k}\cdot\mathbf{r}_2} = e_e e^{i\mathbf{k}\cdot\mathbf{r}_{12}} e^{i\mathbf{k}\cdot\mathbf{r}_1}. \tag{24}$$

In the coordinates $\mathbf{r}_1 = (r_1\cos\varphi_1, r_1\sin\varphi_1)$ and with β as the propagation angle of the plane wave, we have

$$e^{i\mathbf{k}\cdot\mathbf{r}_1} = e^{ikr_1\cos(\varphi_1-\beta)}. \tag{25}$$

By the Jacobi identity [17, eq. (4.1)]

$$\begin{aligned} e^{ikr_1\cos(\varphi_1-\beta)} &= \sum_{n=-\infty}^{\infty} i^n J_n(kr_1) e^{in(\varphi_1-\beta)} \\ &= \sum_{n=-\infty}^{\infty} i^n e^{-in\beta}\hat{\psi}_n(\mathbf{r}_1). \end{aligned} \tag{26}$$

Analogous to the derivation of (23), we take the transmitted field of the plane-wave source $\mathcal{D}_2$ to equal the field that impinges the object $\mathcal{D}_1$. Therefore, the analog of (22) is

$$e^{i\mathbf{k}\cdot\mathbf{r}_2} = \sum_{m=-\infty}^{\infty} S_{m0}^{12}\hat{\psi}_m(\mathbf{r}_1). \tag{27}$$

When we collect (24)–(26), compared to (27), and generalize for all pairs $(\mathcal{D}_i, \mathcal{D}_j)$, where $\mathcal{D}_j$ is a plane-wave source, we have

$$S_{n0}^{ij} = i^n e^{i\mathbf{k}\cdot\mathbf{r}_{ij}} e^{-in\beta_j}. \tag{28}$$

Assuming that all the sources of the electromagnetic fields are explicit in the problem, the total electric field $E_z(\mathbf{r})$ at a given point $\mathbf{r}$, where $\forall j\ \mathbf{r}\notin\mathcal{D}_j$ is the sum of the outbound (i.e., emitted and scattered) fields of all the objects $\mathcal{D}_j$. Therefore,

$$E_z(\mathbf{r}) = \sum_{mj} b_m^j \psi_m(\mathbf{r}_j). \tag{29}$$

An alternative way to evaluate the electric field at a given point $\mathcal{O}_i$ is to posit a nonscattering token object $\mathcal{D}_i$ at the point. The field that impinges $\mathcal{O}_i$ is the sum (29) of the outbound fields of the other objects. On the other hand, the impinging field is given by (5). When we evaluate (5) at $\mathbf{r}_i = 0$ and use $\hat{\psi}_n(0) = \delta_{0n}$ [20, Sec. 10.7(i)], we find

$$E_z(\mathbf{r}_i) = a_0^i, \quad \text{at } \mathbf{r}_i = 0. \tag{30}$$

In summary, the multiple scattering model of the project involves three types of objects: 1) circular scatterers, which may also emit primary fields; 2) plane-wave sources; and 3) token receivers.

C. Dominant Path Approximation

When we require an analytical expression for synthetic beamforming (Section IV-B), it is useful to represent the solution for the multiple scattering problems in terms of separate parts that correspond to the different propagation paths between the objects. Particularly interesting are the propagation paths that lead from the transmitters to the receivers through only a few instances of scattering because the electromagnetic fields that reach the receiver relatively directly suffer the least attenuation from absorption at the interacting objects or from the free-space propagation.

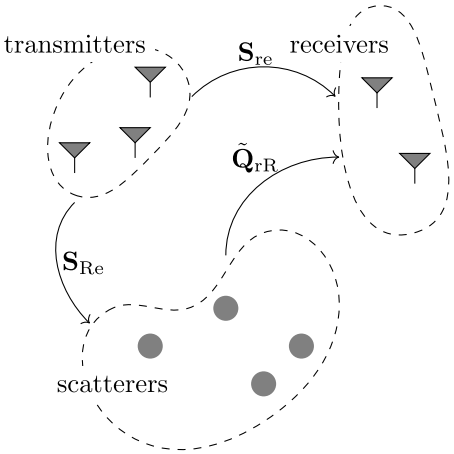

Fig. 4. Antennas and scatterers. The objects of the multiple-scattering model are organized into three groups, similar to [22]. The off-diagonal block matrices of $\mathbf{S}$ in (31) quantify the propagation from one object group to another, whereas the diagonal blocks quantify intragroup propagation. The received signal in (39) is the sum of the signal that propagates from the transmitters to the receivers directly and the signal that reaches the receivers after scattering one or several times from the scattering elements.

We consider a case where the system of objects consists of three groups: the transmitters, the RIS elements, and the receivers (Fig. 4). Because ordering of the indices $1,\ldots,N$ of the N objects has been arbitrary, we can choose to denote the transmitters with the least numbers, the receivers with the greatest ones, and the RIS objects with the numbers in between. With this order of indexing, the matrix $\mathbf{T}$ in (15) and the matrix $\mathbf{S}$ in (18) can be expressed as block matrices

$$\mathbf{T} = \begin{pmatrix} \mathbf{T}_e & & \\ & \mathbf{T}_R & \\ & & \mathbf{T}_r \end{pmatrix}, \quad \mathbf{S} = \begin{pmatrix} \mathbf{S}_{ee} & \mathbf{S}_{eR} & \mathbf{S}_{er} \\ \mathbf{S}_{Re} & \mathbf{S}_{RR} & \mathbf{S}_{Rr} \\ \mathbf{S}_{re} & \mathbf{S}_{rR} & \mathbf{S}_{rr} \end{pmatrix} \tag{31}$$

where the subscripts e, R, and r stand for the transmitter, the RIS, and the receiver, respectively. In contrast to individual objects, for which self-interactions vanish, groups of objects can manifest self-interactions, so that $\mathbf{S}$ in (31) has no explicit vanishing diagonal blocks, even when the vanishing diagonal blocks of $\mathbf{S}$ are explicit in the object-level formula (17).

Because the matrices $\mathbf{S}$ and $\mathbf{T}$ only feature in the system equation of the multiple scattering problem as products $\mathbf{ST}$ and $\mathbf{TS}$, it is convenient to denote the combined effect of scattering and propagation by the following equation:

$$\mathbf{Q} = \mathbf{ST}. \tag{32}$$

If we assume that the transmitters and the receivers interfere with the rest of the objects only weakly, so that $\mathbf{T}_e$ and $\mathbf{T}_r$ vanish, we have

$$\mathbf{Q} = \begin{pmatrix} 0 & \mathbf{Q}_{eR} & 0 \\ 0 & \mathbf{Q}_{RR} & 0 \\ 0 & \mathbf{Q}_{rR} & 0 \end{pmatrix}. \tag{33}$$

It is a matrix identity that when a square matrix $\mathbf{I}-\mathbf{A}$ has invertible square blocks $\mathbf{I}-\mathbf{A}_{ii}$ at its diagonal, the

diagonal blocks can be reduced into identity matrices by the decomposition

$$\mathbf{I}-\mathbf{A}=\left(\mathbf{I}-\tilde{\mathbf{A}}\right)\begin{pmatrix}\mathbf{I}-\mathbf{A}_{00} & 0 & 0\\ 0 & \mathbf{I}-\mathbf{A}_{11} & 0\\ 0 & 0 & \mathbf{I}-\mathbf{A}_{33}\end{pmatrix} \tag{34}$$

where $\tilde{\mathbf{A}}$ has zero matrices along its diagonal. When we use this decomposition to $\mathbf{I}-\mathbf{Q}$, the first equation in (19) becomes

$$\left(\mathbf{I}-\tilde{\mathbf{Q}}\right)\tilde{\mathbf{a}}=\mathbf{S}\mathbf{e} \tag{35}$$

where $\tilde{\mathbf{Q}}$ and $\tilde{\mathbf{a}}$ are of the forms

$$\tilde{\mathbf{Q}}=\begin{pmatrix}0 & \tilde{\mathbf{Q}}_{eR} & 0\\ 0 & 0 & 0\\ 0 & \tilde{\mathbf{Q}}_{rR} & 0\end{pmatrix},\qquad \tilde{\mathbf{a}}=\begin{pmatrix}\mathbf{I} & 0\\ & \mathbf{I}-\mathbf{Q}_{RR}\\ 0 & & \mathbf{I}\end{pmatrix}\mathbf{a}. \tag{36}$$

Those parts of $\mathbf{a}$ and $\tilde{\mathbf{a}}$ that correspond to the electromagnetic fields that impinge the receivers coincide, so that the solutions for (19) and (35) coincide with the received signal.

The benefit of these matrix manipulations is that the improved sparseness of $\tilde{\mathbf{Q}}$ in (36) allows us to write the received field in an intuitive form. When we matrix multiply (35) from the left by $\mathbf{I}+\tilde{\mathbf{Q}}$ and observe that $\tilde{\mathbf{Q}}^2=0$, we have

$$\tilde{\mathbf{a}}=\left(\mathbf{I}+\tilde{\mathbf{Q}}\right)\mathbf{S}\mathbf{e}. \tag{37}$$

If $\mathbf{C}$ is a conversion matrix that determines the conversion of the impinging electromagnetic signal to an electric signal $\mathbf{y}_r$ inside the objects and if we assume that $\mathbf{C}$ only has nonzero entries that correspond to the receiver elements, we have

$$\begin{aligned}\mathbf{y}_r&=\mathbf{C}\mathbf{a}=\begin{pmatrix}0 & 0 & \mathbf{C}_r\end{pmatrix}\mathbf{a}\\ &=\mathbf{C}\tilde{\mathbf{a}}=\mathbf{C}\left(\mathbf{I}+\tilde{\mathbf{Q}}\right)\mathbf{S}\mathbf{e}\end{aligned} \tag{38}$$

which can be written in terms of the blocks of $\tilde{\mathbf{Q}}$ in the explicit form

$$\mathbf{y}_r=\mathbf{C}_r\left(\mathbf{S}_{re}+\tilde{\mathbf{Q}}_{rR}\mathbf{S}_{Re}\right)\mathbf{e}_e. \tag{39}$$

This expression has a simple intuitive meaning. It states that the signal that arrives at the receivers is a combination of the signal that propagates from the transmitter directly and the signal that propagates through the RIS, through the process of multiple scattering (Fig. 4).

IV. Beamforming

An RIS can be used to augment a receiver in a way that makes the directivity of the augmented receiver higher than it would be without the augmentation. In particular, the RIS can enhance or reject plane waves depending on their angle of incidence, when the receiver alone cannot perform this task because of its small size (Fig. 5). In principle, this *spatial filtering* could be implemented by setting the delays of the RIS elements in a way that enhances the primary signal by constructive interference or rejects it by destructive interference, depending on the angle of incidence of the impinging plane wave. However, this implementation of spatial filtering would require that the delay vector $\boldsymbol{\phi}$ can be adjusted continuously, whereas practical implementations of an RIS typically allow only discrete adjustment [8]. To overcome this apparent limitation, we implement the continuous set of delays synthetically, using the multiple scattering models to help the process of synthetic reconstruction (Section IV-B). The goal is to synthesize a beam that approximates a beam of a conventional beamformer (Section IV-A). The beam can be synthesized using analytical formulae (Section IV-B) or numerically (Section IV-D).

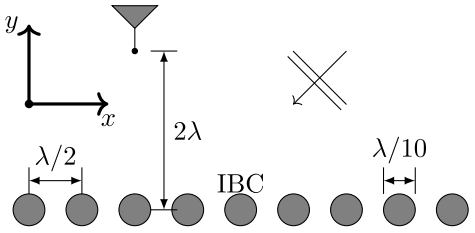

Fig. 5. Beamforming by a linear array of IBC cylinders. Because the IBC cylinders can be programed in a way that implements several configurations of signal delays, the cylinders can effectively act as additional receiver elements, even when they only scatter the fields without registering them. The IBC cylinders form a standard linear array, with the centers of the cylinders separated by the half wavelength $\lambda/2$, where $\lambda=2\pi/k$.

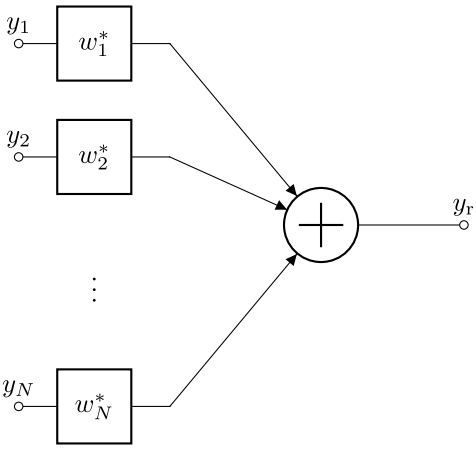

Fig. 6. Conventional beamformer. When a plane wave impinges an array of receivers, the receivers register a vector of input signals, given by (40). The weights w_n^* are chosen so that the beamformer adds the input signals constructively when the plane wave impinges the array from the intended direction.

A. Conventional Beamforming

A conventional receiver array, which consists exclusively of ordinary receiver elements rather than scattering elements, serves as a benchmark for the quality of our synthetic beamforming. In conventional beamforming, the signals that the individual receiver elements observe are weighed by the elements of a vector $\mathbf{w}^H$ and then summed (Fig. 6). In this section, we assume that the impinging wave is plane, with the direction of propagation given by the wave vector $\mathbf{k}=k(\cos\varphi\,\mathbf{u}_x+\sin\varphi\,\mathbf{u}_y)$. If the receiver elements are situated at $\mathbf{r}_1,\ldots,\mathbf{r}_N$ and the value of the impinging plane wave is e_e at a point of reference $\mathbf{r}_0$, the vector of received signals is

$$\begin{pmatrix}y_1\\ \vdots\\ y_N\end{pmatrix}=\begin{pmatrix}e^{i\mathbf{k}\cdot(\mathbf{r}_1-\mathbf{r}_0)}\\ \vdots\\ e^{i\mathbf{k}\cdot(\mathbf{r}_N-\mathbf{r}_0)}\end{pmatrix}e_e\triangleq\mathbf{v}_{\mathbf{k}}(\mathbf{k})e_e \tag{40}$$

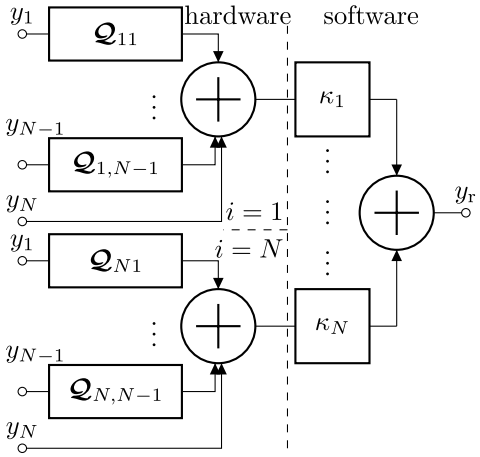

Fig. 7. Synthetic beamformer. The beamformer operates in two stages. First, the hardware cycles through the configurations $i = 1, \ldots, N$ that determine their own beam patterns Υ_i. Second, the software calculates an approximation y_r of the signal that a conventional beamformer with a beam pattern Υ would receive. The coefficients κ_i that enable the mimicking of conventional beamforming are given by beam synthesis. The inputs of the synthetic beamformer depend on the impinging plane wave by (40).

where the vector $\mathbf{v_k}(\mathbf{k})$ accounts for the effect that the array geometry has on the received signal and is referred to as the *array manifold vector* [23, Sec. 2.2]. After the weighed sum of the signals is taken, the total received signal is

$$y_r = \mathbf{w}^H \mathbf{v_k}(\mathbf{k}) e_e = \Upsilon(\mathbf{k}) e_e \tag{41}$$

where the quantity $\Upsilon(\mathbf{k})$ determines the spatial filtering characteristics of the conventional receiver array and is referred to as the *beam pattern*. To obtain conventional beamforming in the direction of a given wave vector $\mathbf{k}_T$, we choose a weight vector

$$\mathbf{w}^H = \frac{1}{N}\left(e^{-i\mathbf{k}_T\cdot(\mathbf{r}_1-\mathbf{r}_0)} \ \ldots \ e^{-i\mathbf{k}_T\cdot(\mathbf{r}_N-\mathbf{r}_0)}\right) \tag{42}$$

so that the individual signal components interfere constructively when $\mathbf{k} = \mathbf{k}_T$ and decoherently otherwise [Fig. 8(a)]. The normalization coefficient $1/N$ guarantees $\Upsilon(\mathbf{k}_T) = 1$.

B. Synthetic Beamforming

We now consider a way to implement spatial filtering that is comparable with that of a conventional beamformer but with only one isotropic receiver element at $\mathbf{r}_N$ and with programmable circular scattering elements at $\mathbf{r}_1, \ldots, \mathbf{r}_{N-1}$. Because the scattering elements switch only to a finite number of states, the array can implement only a finite set of physical beam patterns $\Upsilon_i(\mathbf{k})$. We refer to the process of approximating the beam pattern $\Upsilon(\mathbf{k})$ of a conventional beamformer with a sum $\sum \kappa_i \Upsilon_i(\mathbf{k})$ as *synthetic beamforming* (Fig. 7). We refer to the process of finding the coefficients κ_i as *beam synthesis*.

We assume that each of the objects is small compared to the wavelength while the collection of the objects together spans a distance of several wavelengths. We also assume that any given RIS element $\mathcal{D}_j$ is able to effect a discrete set of phase shifts, which are the same for all the elements. The RIS cycles through a set of N configurations, so that the ith configuration assigns $\mathcal{D}_j$ the phase shift of ϕ_{ij}. If, in the T-matrix of the RIS element, the monopole element that determines the scattering from the small object in the neutral delay configuration is T_{00}^j, the delayed scattering in the ith configuration is determined by $T_{00}^j e^{i\phi_{ij}}$. We can collect the coefficients $e^{i\phi_{ij}}$ into the delay vector

$$\boldsymbol{\phi}_i^T = \left(e^{i\phi_{i1}} \ e^{i\phi_{i2}} \ \ldots \ e^{i\phi_{i(N-1)}}\right) \tag{43}$$

where $i = 1, \ldots, N$ and the first delay vector, which corresponds to the neutral configuration, is $\boldsymbol{\phi}_1^T = \mathbb{1}^T$. Using the small element approximation, we can then take $\mathbf{S}_{rR} = \mathbf{s}_{rR}^T$ to be a row vector in (31). Correspondingly

$$\mathbf{Q}_{rR} = \mathbf{s}_{rR}^T \mathbf{T}_R = \mathbf{q}_{rR}^T$$

which follows from (31) and (32) characterizes $\mathbf{Q}_{rR}$ as a row vector in (33). Then, by effecting the delays, we have

$$\mathbf{q}_{rR,i}^T = \mathbf{s}_{rR}^T \mathbf{T}_R \operatorname{diag}(\boldsymbol{\phi}_i) = \mathbf{q}_{rR}^T \operatorname{diag}(\boldsymbol{\phi}_i). \tag{44}$$

Similarly, we denote the reduced $\tilde{\mathbf{q}}_{rR}$ vector that corresponds to the ith configuration of delays by $\tilde{\mathbf{q}}_{rR,i}$.

As before, the impinging field is assumed plane. The plane wave can be thought of as emanating from a transmitter that is at an infinite distance from the receiver. By (39), the received signal is

$$\begin{aligned} y_r &= C_r\left(s_{re} + \tilde{\mathbf{q}}_{rR}^T \mathbf{s}_{Re}\right) e_e = C_r\left(\tilde{\mathbf{q}}_{rR}^T \ 1\right)\begin{pmatrix}\mathbf{s}_{Re}\\ s_{re}\end{pmatrix} e_e \\ &= C_r\left(\tilde{\mathbf{q}}_{rR}^T \ 1\right)\mathbf{v_k}(\mathbf{k}) e_e. \end{aligned} \tag{45}$$

The equation applies to the neutral delay configuration of the RIS. The beam pattern for the ith configuration is then, by comparison of (45) with (41),

$$\Upsilon_i(\mathbf{k}) = C_r\left(\tilde{\mathbf{q}}_{rR,i}^T \ 1\right)\mathbf{v_k}(\mathbf{k}). \tag{46}$$

Although none of these N beam patterns correspond to the beam pattern of the conventional beamformer, we can make an attempt to construct the conventional beam pattern synthetically from the patterns $\Upsilon_i(\mathbf{k})$ by calculating a weighed sum (Fig. 7). The problem is to find constant coefficients κ_i, so that

$$\Upsilon(\mathbf{k}) = \sum_{i=1}^{N} \kappa_i \Upsilon_i(\mathbf{k}) \tag{47}$$

holds as strictly as possible. We collect the quantities κ_i to a row vector $\boldsymbol{\kappa}^T$ and the vectors $\tilde{\mathbf{q}}_{rR,i}^T$ to a matrix $\boldsymbol{\mathcal{Q}}$. We then have

$$\Upsilon(\mathbf{k}) = C_r \boldsymbol{\kappa}^T \left(\boldsymbol{\mathcal{Q}} \ \mathbb{1}\right)\mathbf{v}_k(\mathbf{k}). \tag{48}$$

Because the equation must hold for all physical values of $\mathbf{k}$, a comparison with (41) gives

$$\mathbf{w}^H = C_r \boldsymbol{\kappa}^T \left(\boldsymbol{\mathcal{Q}} \ \mathbb{1}\right) \tag{49}$$

from which the coefficients κ_i can be obtained numerically by inverting the square matrix $\left(\boldsymbol{\mathcal{Q}} \ \mathbb{1}\right)$.

C. Delay Configurations

Because the beam synthesis methods of Sections IV-B and IV-D only give the vector $\boldsymbol{\kappa}$ of synthesis coefficients with some small error $\delta\boldsymbol{\kappa}$, the synthetic implementation of a particular conventional beamformer will be slightly inaccurate. If the targeted conventional beamformer has the ideal coefficient vector $\mathbf{w}_i$, the synthesis only gives the approximation $\mathbf{w}_a = \mathbf{w}_i + \delta\mathbf{w}$. By (49)

$$\delta\mathbf{w}^H = C_r(\delta\boldsymbol{\kappa})^T\big(\boldsymbol{\mathcal{Q}}\ \mathbb{1}\big).$$

The bound on the relative error in $\mathbf{w}$ is (e.g., [24, Sec. 1.13])

$$\frac{\|\delta\mathbf{w}\|}{\|\mathbf{w}\|} \leq \operatorname{cond}\big(\boldsymbol{\mathcal{Q}}\ \mathbb{1}\big)\frac{\|\delta\boldsymbol{\kappa}\|}{\|\boldsymbol{\kappa}\|}. \tag{50}$$

If we design the augmented receiver in a way that minimizes the condition number in (50), the beam synthesis will be as insensitive as possible to small variations $\delta\boldsymbol{\kappa}$. The goal of the present section is to find a discrete set of delay configurations $\boldsymbol{\phi}_i$ that makes the condition number as small as possible. Again, we use the small element approximation. We also approximate the scattered fields of the elements with single scattering, so that $\mathbf{q}_{rR}$ is used in place of $\tilde{\mathbf{q}}_{rR}$ above (48) in the definition of $\boldsymbol{\mathcal{Q}}$. First, we rearrange (44), so that

$$\mathbf{q}_{rR,i}^T = \mathbf{q}_{rR}^T \operatorname{diag}\big(\boldsymbol{\phi}_i\big) = \boldsymbol{\phi}_i^T \operatorname{diag}(\mathbf{q}_{rR}). \tag{51}$$

The N row vectors $\boldsymbol{\phi}_i^T$ can be arranged into a matrix $\boldsymbol{\Phi}$. The equation then turns into

$$\boldsymbol{\mathcal{Q}} = \boldsymbol{\Phi}\operatorname{diag}(\mathbf{q}_{rR}) \tag{52}$$

so that

$$\big(\boldsymbol{\mathcal{Q}}\ \mathbb{1}\big) = \big(\boldsymbol{\Phi}\ \mathbb{1}\big)\operatorname{diag}\big(\mathbf{q}_{rR}^T\ 1\big). \tag{53}$$

By (1), we then have

$$\operatorname{cond}\big(\boldsymbol{\mathcal{Q}}\ \mathbb{1}\big) \leq \operatorname{cond}\big(\boldsymbol{\Phi}\ \mathbb{1}\big)\operatorname{cond}\big[\operatorname{diag}\big(\mathbf{q}_{rR}^T\ 1\big)\big] \tag{54}$$

from which we see that progress in minimizing the relevant condition number can be made by carefully designing the discrete set of delays $\boldsymbol{\Phi}$, so that the first condition number on the right-hand side of (54) is minimized.

Hardware limitations determine the strategy of constructing $\boldsymbol{\Phi}$. As in Section IV-B, we assume that in the augmented receiver, there are $N-1$ RIS elements and a single receiver element. Furthermore, we assume that the RIS elements are nonabsorbing and switch into N possible states. The design problem is to choose the N nonabsorbing states and the sequence in which they are applied to the RIS elements in a way that minimizes the condition number of $\big(\boldsymbol{\Phi}\ \mathbb{1}\big)$. One solution is to set

$$\boldsymbol{\Phi} = \big[\zeta^{(i-1)j}\big], \qquad i = 1,\ldots,N,\ j = 1,\ldots,N-1 \tag{55}$$

where $\zeta = e^{-2\pi i/N}$. In this case, $\big(\boldsymbol{\Phi}\ \mathbb{1}\big)$ is the *discrete Fourier transform* (DFT) matrix[1] [25, Sec. 1.4.1], with the first column moved to the end of the matrix. A scalar multiple of $\big(\boldsymbol{\Phi}\ \mathbb{1}\big)$ is then unitary, so that

$$\big(\boldsymbol{\Phi}\ \mathbb{1}\big)^H\big(\boldsymbol{\Phi}\ \mathbb{1}\big) = N\mathbf{I}$$

which implies that $\big(\boldsymbol{\Phi}\ \mathbb{1}\big)$ has a unit condition number.

[1]In the literature, the DFT matrix is used in computing the DFT [25].

If the hardware limitations are even more stringent—so that the RIS elements only switch between two states, both of which are nonabsorbing—the design goal can be met by choosing the first state to have a neutral phase shift $\phi = 0$ and the second state a half-wave phase shift $\phi = \pi$. If the number of elements in the augmented receiver is of the form $N = 2^M$, we can construct an orthogonal $\big(\boldsymbol{\Phi}\ \mathbb{1}\big)$ with the Hadamard matrix [26, Sec. 2.7]. For example, we could have

$$\big(\boldsymbol{\Phi}\ \mathbb{1}\big) = \begin{pmatrix} 1 & 1 & 1 & 1 \\ -1 & 1 & -1 & 1 \\ 1 & -1 & -1 & 1 \\ -1 & -1 & 1 & 1 \end{pmatrix} \tag{56}$$

when $N = 4$. More generally, $\big(\boldsymbol{\Phi}\ \mathbb{1}\big)$ for $N = 2^M$ is constructed from the $N \times N$ Hadamard matrix $\mathbf{H}_N$ by permuting the set of columns of $\mathbf{H}_N$ cyclically, so that the first column of $\mathbf{H}_N$ becomes the final column of $\big(\boldsymbol{\Phi}\ \mathbb{1}\big)$. A scalar multiple of the matrix is orthogonal, which implies that the matrix has a unit condition number.

D. Numerical Weights

After the beam synthesis, the coefficients κ_i determine the pattern of the synthetic beam by (47). The beam synthesis only needs to be performed again if the beam pattern requires an adjustment. If the beam pattern is only adjusted infrequently, the algorithm that computes κ_i is not time-sensitive and requires no careful optimization for efficiency. Therefore, alternative algorithms that perform less efficiently than the beam synthesis algorithm of Section IV-B can become useful. In particular, we consider an algorithm that computes κ_i numerically, without analytically derived expressions for the row vectors $\tilde{\mathbf{q}}_{rR,i}^T$ of the matrix $\boldsymbol{\mathcal{Q}}$ in (49). In addition to its practical use, the numerical algorithm can help corroborate the beam synthesis algorithm of Section IV-B.

The starting point for the numerical beam synthesis is (46). When we apply this equation for the different delay configurations, indexed with $i = 1,\ldots,N$, and for different wave vectors $\mathbf{k}_j$, where $j = 1,\ldots,M$, and collect the results into a matrix equation, we get

$$\boldsymbol{\Upsilon} = C_r\big(\boldsymbol{\mathcal{Q}}\ \mathbb{1}\big)\begin{pmatrix}\mathbf{V}\\ \mathbf{v}^T\end{pmatrix} \tag{57}$$

where, with row indices i and column indices j,

$$\boldsymbol{\Upsilon} = \big[\Upsilon_i(\mathbf{k}_j)\big], \quad \begin{pmatrix}\mathbf{V}\\ \mathbf{v}^T\end{pmatrix} = \big[\mathbf{v}_{\mathbf{k}}(\mathbf{k}_j)\big]. \tag{58}$$

If $\boldsymbol{\Upsilon}$ is known independent of (57), we can solve (57) for the matrix $\boldsymbol{\mathcal{Q}}$ without first constructing the vectors $\tilde{\mathbf{q}}_{rR}$ that Section IV-B used. This avoids some complexity but with the expense of a more intense numerical computation. To get $\boldsymbol{\Upsilon}$ without explicitly using (57), we note that a comparison between (38) and (39) allows us to write (45) as $y_r = C_r a_0^N$ and consequently (46) as follows:

$$\Upsilon_i(\mathbf{k}_j) = \frac{C_r a_{0,i}^N(\mathbf{k}_j)}{e_e} \tag{59}$$

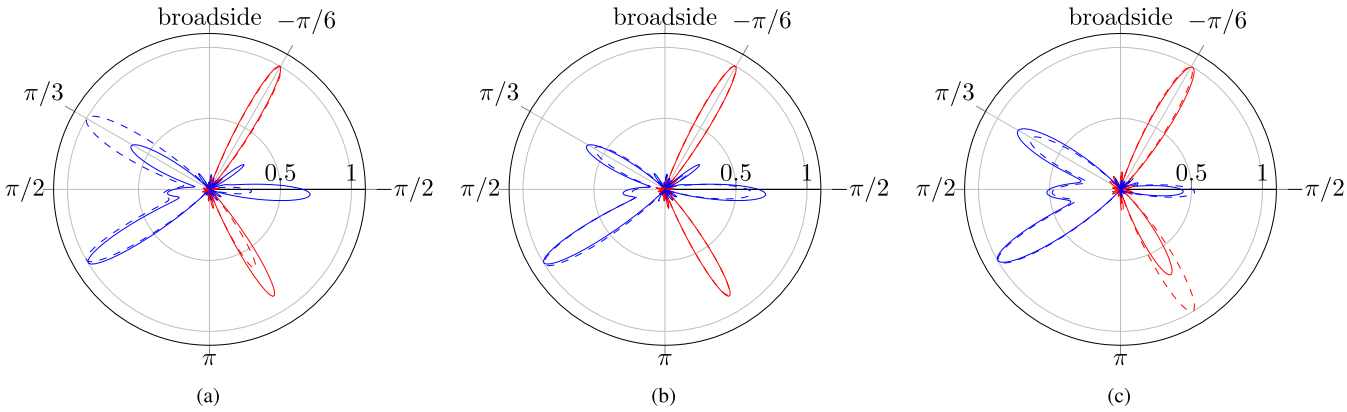

Fig. 8. Comparisons between various methods of beamforming. The array of Fig. 5 was used. All curves represent the squared absolute value $|y_r(\bar{\varphi})|^2$ of the received signal, considered as a function of the incidence angle $\bar{\varphi} = \varphi - \pi/2$ of (63) and normalized for a unit maximum value. To test the beamformers, we used each method to implement two beams: one directed $\pi/3$ to the left from the broadside and another directed $\pi/6$ to the right from the broadside. (a) Conventional (– –, – –) and synthetic (——, ——) beamforming. The beam synthesis works more accurately when the beam direction deviates from the broadside only moderately. (b) Numerical (– –, – –) and analytical (——, ——) syntheses. (c) Synthesis with Hadamard (– –, – –) and DFT (——, ——) matrices. For this last comparison, the RIS of Fig. 5 was truncated from the right into only seven elements.

where the coefficient a_0^N has been represented as a function of the wave vector $\mathbf{k}_j$ and the delay configuration $\boldsymbol{\phi}_i$. When we solve (19) for the different delay configurations $\boldsymbol{\phi}_i$ and wave vectors $\mathbf{k}_j$ to get the coefficients $a_{0,i}^N$, we get $\Upsilon_i(\mathbf{k}_j)$ from (59). When we perform the block matrix multiplication in (57) and rearrange, we get

$$\mathcal{Q}\mathbf{V} = \frac{1}{C_r}\Upsilon - \mathbb{1}\mathbf{v}^T. \tag{60}$$

By the matrix multiplication rule, $\mathbb{1}\mathbf{v}^T$ is a matrix with N copies of the row vector $\mathbf{v}^T$. The right-hand side of the equation has an intuitive interpretation. It is the contribution of the RIS elements on the beam pattern, scaled with C_r. The matrix $\mathbf{V}$ is generally rectangular and therefore is not guaranteed to have an inverse. In fact, taking the number M of different $\mathbf{k}_j$ to be larger than the number N of different $\boldsymbol{\phi}_i$ proves, by numerical experiment, to be advantageous for the quality of the beam synthesis, even when $M > N - 1$ results in a rectangular matrix. In the general case, we multiply both sides of the equation from the right by the pseudoinverse $\mathbf{V}^\dagger = \mathbf{V}^H(\mathbf{V}\mathbf{V}^H)^{-1}$. Explicitly

$$\mathcal{Q} = \left(\frac{1}{C_r}\Upsilon - \mathbb{1}\mathbf{v}^T\right)\mathbf{V}^\dagger. \tag{61}$$

When we find $\mathcal{Q}$ by the formula and use it in (49), we again get the coefficients κ_i, like in Section IV-B. The main difference between the two approaches is the compromise between parsimony and performance.

V. Results

A. Beamforming

Although the theory of Sections III-A and III-B does not limit the geometry of the augmented receiver, apart from requiring that the elements be circular cylinders, the simple geometry of a linear array was chosen for an illustration (Fig. 5). In the array, the nine RIS elements are organized in a linear arrangement and spaced at half-wave distances, where the distance is taken between the centers. The radius of the circular RIS elements was chosen to be 0.05 wavelengths, so that it was justified to use the small element approximation that is assumed in the beam synthesis of Section IV-B. The final element of the augmented receiver is the receiver element, which is placed in front of the RIS, like in Fig. 5. For the delay configuration matrix $\boldsymbol{\Phi}$, the permuted DFT matrix of Section IV-C was chosen.

Because Section IV-B adopted conventional beamforming as the benchmark for synthetic beamforming, we compare the synthesized beam with the conventional beam in our test case that involves the linear array. Fig. 8(a) shows that the mainlobe of the synthetic beam is correctly oriented, whether the target direction is $\pi/3$ radians counterclockwise from the broadside of the array or $\pi/6$ radians clockwise. Because the synthesized receiver array consists mostly of a linear array, it more precisely resolves the wave vector component $\mathbf{k} \cdot \mathbf{u}_x$ that lies along the axis of the linear part of the array than the perpendicular component $\mathbf{k} \cdot \mathbf{u}_y$. Therefore, sidelobes emerge that constitute approximate mirror images of the mainlobes. These mirror images are not precise copies of the mainlobes because the receiver element, which is offset from the array axis, breaks the reflection symmetry of the augmented receiver (Fig. 5).

Because a synthetic beamformer uses more limited hardware than a conventional beamformer, the quality of the beam pattern is expected to be moderately compromised. Indeed, Fig. 8(a) shows that the directivity of the synthetic beam is lower than that of the conventional beam and that the sidelobes of the synthetic beam are comparatively large. However, beam synthesis still produces a beam that can be recognized as a modified version of the conventional beam. Therefore, the synthetic beamformer is useful in spatial filtering.

Two methods of beam synthesis were discussed in Sections IV-B and IV-D: analytical and numerical. The synthesized beams of each method are illustrated in Fig. 8(b). The difference between the two methods is only significant for the beam that is oriented to the left from the broadside. For this beam, the analytically synthesized beam offers slightly better directivity than the numerically synthesized one. Therefore, the

analytical method has the advantage that the synthesis is faster to compute—with approximately 50-fold speedup with our software implementation and hardware—and the beam pattern turns out to be moderately superior. The way that the results of both methods nearly coincide suggests that the methods are valid within their domain of application, that is, when the RIS elements are sufficiently small. Also, the way that both methods fall short of precisely reproducing the conventional beam suggests that the hardware limitations inherently require some compromise in the directivity of the beam.

Finally, we compare the performances of the two types of delay matrices—DFT and Hadamard—that were discussed in Section IV-C. In our implementation, we can only model the delay matrix after the Hadamard matrix if the number of elements in the augmented receiver is of the form $N = 2^M$. Therefore, the augmented receiver of Fig. 5 has to be truncated by two elements. When we remove the two rightmost RIS elements of the array, we find that the synthetic beams are like in Fig. 8(c). The approach that uses the Hadamard matrix results in less directivity than what can be obtained using the DFT matrix. However, applications are likely to arise that benefit from exchanging some performance for the cost efficiency that a simpler physical implementation of the beamformer permits.

Although the small element approximation is used in beam synthesis—that is, to compute the coefficients κ_i—the beam patterns of Fig. 8(a) and (b), which correspond to given coefficients κ_i, were computed with the full precision of the multiple scattering model. Therefore, only the accuracy to which the conventional beamformer is mimicked by the synthetic beamformer depends on the degree of validity in the small element approximation, whereas the accuracy to which the beam patterns were computed in Fig. 8(a) and (b) is unaffected by the approximation.

B. Performance Measure

The shape of the beam pattern generally depends on the target angle φ_T. We find it convenient to plot the results as a function of the incidence angle $\bar{\varphi} = \varphi - \pi/2$ rather than the grazing angle φ. In Fig. 8(a), we observe that the synthetic beam toward $\bar{\varphi}_T = -\pi/6$ has a more distinct mainlobe than the synthetic beam toward $\bar{\varphi}_T = \pi/3$. The distinctness of the mainlobe is one possible performance measure for a beam. It is quantified by the concept of *directivity* [23, Sec. 2.6.1]. We denote the beam that is oriented toward the direction $\bar{\varphi}_T$ by the following equation:

$$\Upsilon_{\bar{\varphi}_T}(\bar{\varphi}) = \Upsilon_{\mathbf{k}_T}(\mathbf{k}) \tag{62}$$

where

$$\begin{aligned} \mathbf{k} &= -k\big(\cos\bar{\varphi}\mathbf{u}_y - \sin\bar{\varphi}\mathbf{u}_x\big) \\ \mathbf{k}_T &= -k\big(\cos\bar{\varphi}_T\mathbf{u}_y - \sin\bar{\varphi}_T\mathbf{u}_x\big). \end{aligned} \tag{63}$$

The minus sign arises because of the inward pointing direction of the vector $\mathbf{k}$. In analogy to the usual directivity in 3-D, we define the 2-D directivity as follows:

$$D(\bar{\varphi}_T) = \frac{\sup_{\bar{\varphi}} |\Upsilon_{\bar{\varphi}_T}(\bar{\varphi})|^2}{\frac{1}{2\pi}\int_0^{2\pi} |\Upsilon_{\bar{\varphi}_T}(\bar{\varphi})|^2 \,\mathrm{d}\bar{\varphi}} \tag{64}$$

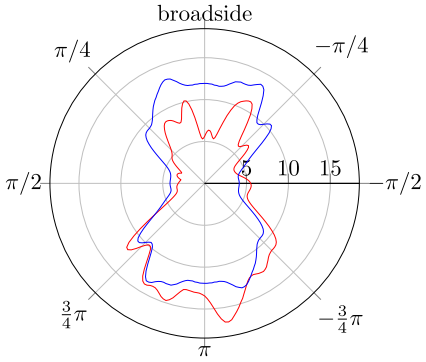

Fig. 9. Directivity as function of target angle $\bar{\varphi}_T$. The directivity of the conventional beam (——) only coincides with that of the synthetic beam (——) approximately. The synthetic beam is sharper at the backside of the RIS than at the front side. The conventional beam is equally sharp on both sides.

where the supremum $\sup_{\bar{\varphi}} |\Upsilon_{\bar{\varphi}_T}(\varphi)|^2$ is evaluated on a small angular spread $[\bar{\varphi}_T - \Delta\bar{\varphi}, \bar{\varphi}_T + \Delta\bar{\varphi}]$ to account for a possible deviation of the beam maximum from the target direction $\bar{\varphi}_T$ and for a possible sidelobe that exceeds the mainlobe in magnitude. Because, in 2-D, the directivity of the standard linear array declines when the beam is steered away from the broadside, we could expect the same for the synthetic beam of the receiver in Fig. 5. Indeed, Fig. 9 shows that both the conventional and the synthetic beams suffer a decline in their directivities when $\bar{\varphi}_T$ is close to $\pi/2$ or $-\pi/2$—that is, the *endfire* directions.

Although the directivity of the synthetic beam resembles that of a conventional beam in Fig. 9—especially on the lower semicircle of the diagram—some differences between the two types of beams can also be observed. The directivity of the synthetic beam varies significantly near the broadside direction on the upper semicircle of the diagram. The variation is particularly significant in contrast to that in the directivity of the conventional beam, which varies only moderately near the broadside direction.

The beam of a conventional beamformer has the symmetry

$$\Upsilon_{-\mathbf{k}_T}(\mathbf{k}) = \Upsilon^*_{\mathbf{k}_T}(-\mathbf{k}) \tag{65}$$

from which $D(\bar{\varphi}_T) = D(\bar{\varphi}_T + \pi)$ follows. This symmetry is also manifest in Fig. 9. However, the synthetic beam does not have the same symmetry because the synthetic beam approximates the conventional one only roughly.

It follows from the symmetry (65) that the conventional beamformer works equally well whether its beam is steered toward the front side—that is, that half-plane that borders the linear part of the receiver array and contains the solitary receiver antenna that does not align with the others—or to the backside. However, the RIS-augmented receiver differs from a conventional beamformer by scattering the impinging field instead of merely registering it. This, indeed, explains the loss of symmetry in Fig. 9. The upper and the lower semicircles of Fig. 9 illustrate two possible modes of operation for the RIS-augmented receiver of Fig. 5.

1) When the RIS is steered toward the front side, it reflects the target plane wave to the receiver antenna.
2) When the RIS is steered toward the backside, the target plane wave diffracts through it to the receiver.

We observe that, in contrast to the conventional beam, the synthetic beam has better directivity on the backside than on the front side.

VI. Conclusion

This article introduced a model for designing an RIS-augmented receiver that emulates the operation of a conventional beamformer by beam synthesis. The quality of the synthetic beam turned out to be satisfactory, even when the strict design constraints made it impossible to precisely reproduce the beam of a conventional beamformer. The match between the synthetic beam and the conventional beam was proximate when the beam was steered only slightly away from the broadside while the deterioration of the beam could not be avoided when the deviation of the beam direction from the broadside was remarkable [Fig. 8(a)].

To keep a suitably narrow focus, the article confined itself to the discussion of circular cylinders. However, cylinders of other shapes are easily within the reach of the T-matrix method [27]. The main distinction of a discussion of the general cylinders to that of the circular ones is that the corresponding T-matrices would no longer be diagonal in the more general case and would need to be computed by separate methods, independent of (10).

Because the article assumes, for simplicity, that the circular cylinders are infinitely long, we do not propose the geometry as a practical implementation of RIS. Practical designs require an elaborate 3-D electromagnetic scattering model, which remains a topic for further research.

References

[1] E. Basar, M. Di Renzo, J. De Rosny, M. Debbah, M.-S. Alouini, and R. Zhang, "Wireless communications through reconfigurable intelligent surfaces," *IEEE Access*, vol. 7, pp. 116753–116773, 2019.

[2] M. Di Renzo et al., "Smart radio environments empowered by reconfigurable intelligent surfaces: How it works, state of research, and the road ahead," *IEEE J. Sel. Areas Commun.*, vol. 38, no. 11, pp. 2450–2525, Jul. 2020.

[3] Q. Wu and R. Zhang, "Intelligent reflecting surface enhanced wireless network: Joint active and passive beamforming design," in *Proc. IEEE Global Commun. Conf. (GLOBECOM)*, Dec. 2018, pp. 1–6.

[4] O. Özdogan, E. Björnson, and E. G. Larsson, "Intelligent reflecting surfaces: Physics, propagation, and pathloss modeling," *IEEE Wireless Commun. Lett.*, vol. 9, no. 5, pp. 581–585, May 2020.

[5] E. Björnson, Ö. Özdogan, and E. G. Larsson, "Reconfigurable intelligent surfaces: Three myths and two critical questions," *IEEE Commun. Mag.*, vol. 58, no. 12, pp. 90–96, Dec. 2020.

[6] V. Jamali, H. Ajam, M. Najafi, B. Schmauss, R. Schober, and H. V. Poor, "Intelligent reflecting surface assisted free-space optical communications," *IEEE Commun. Mag.*, vol. 59, no. 10, pp. 57–63, Oct. 2021.

[7] J. Hu et al., "Reconfigurable intelligent surface based RF sensing: Design, optimization, and implementation," *IEEE J. Sel. Areas Commun.*, vol. 38, no. 11, pp. 2700–2716, Nov. 2020.

[8] C. You, B. Zheng, and R. Zhang, "Intelligent reflecting surface with discrete phase shifts: Channel estimation and passive beamforming," in *Proc. IEEE Int. Conf. Commun. (ICC)*, Jun. 2020, pp. 1–6.

[9] D. Dardari, "Communicating with large intelligent surfaces: Fundamental limits and models," *IEEE J. Sel. Areas Commun.*, vol. 38, no. 11, pp. 2526–2537, Nov. 2020.

[10] W. Tang et al., "Wireless communications with reconfigurable intelligent surface: Path loss modeling and experimental measurement," *IEEE Trans. Wireless Commun.*, vol. 20, no. 1, pp. 421–439, Jan. 2021.

[11] M. A. ElMossallamy, H. Zhang, L. Song, K. G. Seddik, Z. Han, and G. Y. Li, "Reconfigurable intelligent surfaces for wireless communications: Principles, challenges, and opportunities," *IEEE Trans. Cognit. Commun. Netw.*, vol. 6, no. 3, pp. 990–1002, Sep. 2020.

[12] M. Di Renzo, F. H. Danufane, and S. Tretyakov, "Communication models for reconfigurable intelligent surfaces: From surface electromagnetics to wireless networks optimization," *Proc. IEEE*, vol. 110, no. 9, pp. 1164–1209, Sep. 2022.

[13] S. Shen, B. Clerckx, and R. Murch, "Modeling and architecture design of reconfigurable intelligent surfaces using scattering parameter network analysis," *IEEE Trans. Wireless Commun.*, vol. 21, no. 2, pp. 1229–1243, Feb. 2022.

[14] J. C. B. Garcia, A. Sibille, and M. Kamoun, "Reconfigurable intelligent surfaces: Bridging the gap between scattering and reflection," *IEEE J. Sel. Areas Commun.*, vol. 38, no. 11, pp. 2538–2547, Nov. 2020.

[15] E. Bjornson, O. T. Demir, and L. Sanguinetti, "A primer on near-field beamforming for arrays and reconfigurable intelligent surfaces," in *Proc. 55th Asilomar Conf. Signals, Syst., Comput.*, Oct. 2021, pp. 105–112.

[16] P. Mei et al., "On the study of reconfigurable intelligent surfaces in the near-field region," *IEEE Trans. Antennas Propag.*, vol. 70, no. 10, pp. 8718–8728, Oct. 2022.

[17] P. A. Martin, *Multiple Scattering: Interaction of Time-Harmonic Waves With N Obstacles*. Cambridge, U.K.: Cambridge Univ. Press, 2006.

[18] J. A. Stratton, *Electromagnetic Theory*. Hoboken, NJ, USA: Wiley, 2007.

[19] I. V. Lindell and A. Sihvola, *Boundary Conditions in Electromagnetics*. Hoboken, NJ, USA: Wiley, 2020.

[20] F. Olver, D. Lozier, R. Boisvert, and C. Clark, *NIST Handbook of Mathematical Functions*. New York, NY, USA: Cambridge Univ. Press, 2010.

[21] I. Lindell and K. Nikoskinen, *Sähkömagnetiikka*. Espoo, Finland: Department of Radio Science and Engineering, 2011.

[22] T. Pedersen, G. Steinböck, and B. H. Fleury, "Modeling of reverberant radio channels using propagation graphs," *IEEE Trans. Antennas Propag.*, vol. 60, no. 12, pp. 5978–5988, Dec. 2012.

[23] H. L. Van Trees, *Optimum Array Processing*. New York, NY, USA: Wiley, 2002.

[24] J. G. Van Bladel, *Electromagnetic Fields*, 2nd ed. Hoboken, NJ, USA: Wiley, 2007.

[25] G. H. Golub and C. F. Van Loan, *Matrix Computations*, 4th ed. Baltimore, MD, USA: The Johns Hopkins Univ. Press, 2013.

[26] L. N. Trefethen and D. Bau, *Numerical Linear Algebra*. Philadelphia, PA, USA: Society for Industrial and Applied Mathematics, 1997.

[27] D. Felbacq, G. Tayeb, and D. Maystre, "Scattering by a random set of parallel cylinders," *J. Opt. Soc. Amer. A, Opt. Image Sci.*, vol. 11, no. 9, pp. 2526–2538, Sep. 1994.

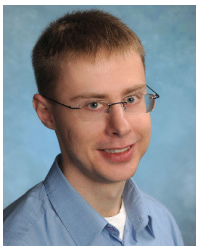

Tommi E. Rimpiläinen received the M.Sc.(tech.) and D.Sc.(tech.) degrees (Hons.) in electrical engineering from Aalto University, Espoo, Finland, in 2011 and 2016, respectively.

From 2019 to 2020, he was a Visiting Researcher at the Photonics Initiative, Advanced Science Research Center (ASRC), City University of New York (CUNY), New York, NY, USA. He is currently a Researcher at the Department of lnformation and Communications Engineering (DICE), School of Electrical Engineering, Aalto University. His research interests include the applications of electromagnetic scattering models in remote sensing, photonics, and communication networks.

Riku Jäntti (Senior Member, IEEE) received the M.Sc.(tech.) degree (Hons.) in electrical engineering and the D.Sc.(tech.) degree (Hons.) in automation and systems technology from the Helsinki University of Technology (TKK), Espoo, Finland, in 1997 and 2001, respectively.

Until 2006, he was a pro tempore Professor at the Department of Computer Science, University of Vaasa, Vaasa, Finland. He is currently a Full Professor of Communications Engineering at the Department of lnformation and Communications Engineering (DICE), School of Electrical Engineering, Aalto University, Espoo. His research interests include radio resource control and optimization for machine-type communications, cloud-based radio access networks, radio frequency inference, ambient backscatter communication, and quantum communications.

Prof. Jäntti is an Associate Editor of IEEE Transactions on Cognitive Communications and Networking.